



Cryogenic forming behaviour of AW-6016-T4 sheet

M. KUMAR¹, N. SOTIROV^{1,2}, F. GRABNER¹, R. SCHNEIDER³, G. MOZDZEN⁴

1. LKR Leichtmetallkompetenzzentrum Ranshofen GmbH,

Austrian Institute of Technology, Postfach 26, 5282 Ranshofen, Austria;

2. BENTELER Automobiltechnik GmbH, An der Talle 27-31, 33102 Paderborn, Germany;

3. Voestalpine Polynorm GmbH & Co. KG, Polynormstraße 1, 73529 Schwäbisch Gmünd, Germany;

4. Aerospace & Advanced Composites GmbH, Viktor-Kaplan-Strasse 2, 2700 Wiener Neustadt, Austria

Received 26 April 2016; accepted 21 September 2016

Abstract: The objective of this work is to study the cryogenic sheet metal forming behaviour of precipitation hardening AW-6016-T4. In this regard, the flow curves and forming limit curves were obtained by tension and Nakazima experimental testing methods in the temperature ranges from -196 to 25 °C. It was found that strength and elongation increase with decreasing temperature. Small but perceived differences between microstructure of the material deformed at the room and cryogenic temperatures respectively were identified by electron backscatter diffraction (EBSD) analysis. However, no significant difference in the precipitation kinetics during continuous heating in the DSC has been observed. This study has demonstrated the potential of cryogenic forming by manufacturing a B-pillar part with 8 mm depth of side design element as compared to 6 mm at room temperature.

Key words: AW-6016-T4 alloy; cryogenic forming; strain hardening; forming limit curve

1 Introduction

Lightweight materials such as aluminium alloys are playing an important role in the weight reduction of vehicles. However, their limited formability at room temperature presents a major challenge and limits their adoption in the industry.

Significant formability improvements may be obtained from the recovery annealing [1], retrogression forming [2], warm forming [3–5], hot stamping [6,7] and superplastic forming [8], heat-assisted forming approaches. But, this improvement in formability comes at the expense of the sheet strength. Due to the combined effect of heat and plastic deformation, the reduction in strength is mainly associated with the dissolution of hardening precipitates, and is also the result of recovery and recrystallization in the microstructure.

In order to avoid the associated microstructural changes caused by heat assisted plastic deformation, aluminium sheets may be deformed at cryogenic temperatures [9]. The general increase in strength, ductility and forming limits at cryogenic temperatures down to -196 °C for AW-5182-O sheet alloy has recently

been reported by SOTIROV et al [10]. They observed that the AW-5182 alloy sheet at room temperature (RT) exhibited poor surface quality due to the appearance of stretcher strain markings, also known as the Portevin–LeChatelier (PLC) effect. SCHNEIDER et al [11] have reported that the PLC effect can be significantly suppressed by forming the AW-5182 sheet at cryogenic temperatures.

These improvements in the formability, strength and surface quality of AW-5182 alloy sheet via cryogenic sheet metal forming encourage the testing of other automotive aluminium sheet such as AW-6016-T4. The characterisation of the material behaviour plays an essential role for subsequent feasibility studies. Therefore, in this work, AW-6016-T4 sheet is characterized over the temperature range from -196 to 25 °C by uniaxial tension and Nakazima tests to investigate the forming behaviour. In order to demonstrate the possibility of applying the low temperature forming technology in the production of a representatively shaped car body part, a coolable B-pillar forming tool was designed and the corresponding forming tests were carried out. Microstructures of the material deformed at room and cryogenic temperatures

were evaluated by electron backscatter diffraction (EBSD) and differential scanning calorimetry (DSC) analysis.

2 Experimental

2.1 Tension tests

The flow curves of AW-6016-T4 sheet were measured on a Zwick Z100 universal testing machine at temperatures between RT and $-196\text{ }^{\circ}\text{C}$ and at strain rates of 0.001 and 0.05 s^{-1} . Tensile tests were carried out in a chamber installed on the testing machine. Cooling of the samples was performed by spraying liquid nitrogen into the chamber until the desired sample temperature was reached. The temperature was measured at two locations: the gas temperature in the chamber and the sample holder temperature. When both temperatures were in equal, the experiment was started. For measurements at $-196\text{ }^{\circ}\text{C}$, the tests were carried out in a bath of liquid nitrogen and both the sample and sample holder were completely submerged during the test. Important parameters from the flow curve measured during the tension test were determined as follows:

$$\sigma_y = \sigma_{0.2} \quad (1)$$

$$\theta = d\sigma/d\varepsilon \quad (2)$$

where σ_y is the yield strength, $\sigma_{0.2}$ is the stress at 0.2% offset true strain, θ is the instantaneous strain hardening rate. σ and ε are true stress and true plastic strain, respectively.

The instantaneous work-hardening rate was determined by numerically differentiating the true stress–true plastic strain data.

2.2 Nakajima tests

Forming limit curves were recorded at room temperature, $-50\text{ }^{\circ}\text{C}$ and $-100\text{ }^{\circ}\text{C}$ using the Nakajima test method. The Nakajima forming tests were conducted according to ISO12004 on an Interlaken Servo Press 225. In order to ensure even cooling of the specimen, the punch, blank holder and die were cooled with liquid

nitrogen. Sample, material and test parameters for a Nakajima cryogenic test are given in Fig. 1 and Table 1, respectively and for each test the specimens were cooled and tested within 180 s. The sheet metal samples were all 250 mm long, but with different widths (20, 50, 80, 100 and 250 mm). During the test, an ARAMIS optical strain measuring system was used to record the history of the deformation field.

Integrated adjustable secondary design elements (SDEs) were designed to be able to show the individual forming limits at different temperatures for the AA6016 in the B-pillar component. Figure 2 shows the punch of the coolable B-pillar forming tool with the integrated SDEs ranging from heights of 4 to 10 mm along with formed B-pillar. These B-pillar forming tests were carried out in a Neff 1600 kN hydraulic press and the punch, blank-holder and die were actively cooled using

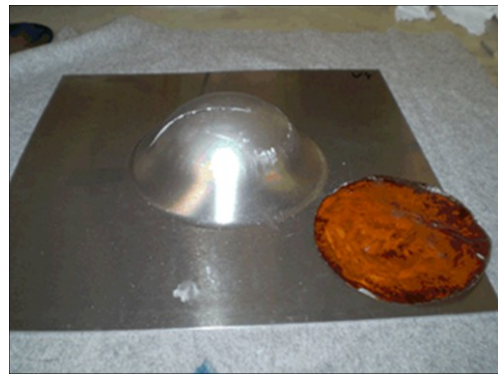


Fig. 1 Full Nakajima tested sample with lubricant along with material

Table 1 Test parameters for Nakajima cryogenic test

Parameter	Value
Alloy-temper	AW-6016-T4
Sheet thickness/mm	1.0
Lubricant	Foil + oil based lubricant
Punch/die diameter/mm	100/105
Forming temperature/ $^{\circ}\text{C}$	RT, -50 , -100
Test speed/($\text{mm} \cdot \text{min}^{-1}$)	90
Blank holder force/kN	400

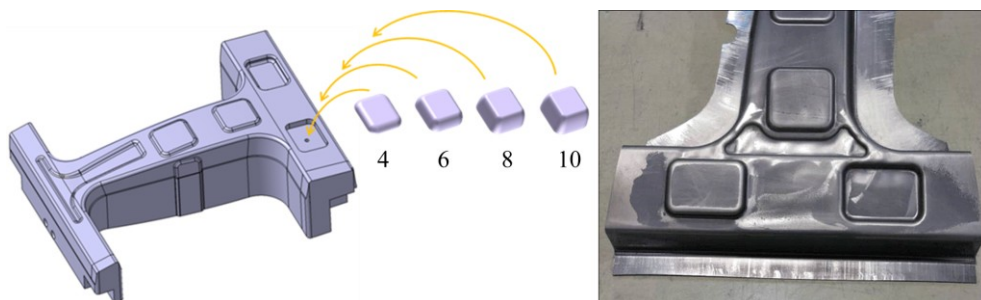


Fig. 2 Punch of B-pillar tool with schematic illustration of adjustable SDEs (4 to 10 mm) along with formed B-pillar

liquid nitrogen up to $-150\text{ }^{\circ}\text{C}$. In the case of the forming tests conducted at temperatures T lower than RT, the sheet was direct contact cooled for 60 s in the closed tool (blank holder to die) before drawing. To avoid any temperature gradients towards the centre of the B-pillar blank surface during the cooling process, the punch was additionally lowered into position right at the blank (ensuring direct contact). Further, the sheet metal forming was carried out as a 1-stage process at a forming velocity of 10 mm/s.

2.3 Differential scanning calorimetry

DSC samples were prepared from the AW-6016-T4 sheet in different conditions. These tests were carried out using a Netzsch-DSC 204 F1 differential scanning calorimeter in which the samples were continuously heated up to $600\text{ }^{\circ}\text{C}$ with a heating rate of 10 K/min. The DSC samples were stamped from as-received AW-6016-T4 sheet as well as from the middle of the gauge length of tensile specimen deformed 20% at RT and $-196\text{ }^{\circ}\text{C}$. These tests provided information about the initial precipitation state of the alloy in the as-received state and after the thermo-mechanical treatment.

2.4 Electron back scatter diffraction

EBSD analysis has been performed on electro-polished specimens with an AMETEK-EDAX detector integrated in a HRSEM ZEISS Supra 40 VP. When preparing the specimens, special care was taken in order to avoid deformation of the surfaces to be analysed. The Kikuchi-patterns were recorded at an accelerating voltage of 20 kV and a specimen tilt-angle of 70° using TSL OIM Data Collection Software. For each material condition, two scans (one vertical and one parallel to longitudinal axis of the tensile test specimen) have been collected. Each scan encompassed an area of $150\text{ }\mu\text{m} \times 300\text{ }\mu\text{m}$ recorded with a step size of 200 nm and the analysis of the raw data was performed using the TSL OIM Analysis Software. For all scans, a clean-up procedure including grain dilation with minimum grain size of 5 pixels has been applied.

3 Results and discussion

Figure 3 shows the true stress–true plastic strain curves for the AW-6016 sheet in T4 condition tested at temperatures between -196 and $25\text{ }^{\circ}\text{C}$ and at the strain rates of 0.001 and 0.05 s^{-1} . A substantial increase in true stress and true plastic strain can be observed with decreasing temperature from RT to $-196\text{ }^{\circ}\text{C}$. It is interesting to note that the strain rate has no significant influence on the flow behaviour. The instantaneous strain hardening rate, $d\sigma/d\varepsilon$ and reduced true stress, $(\sigma-\sigma_y)$ were determined from the flow curves and are shown in

Fig. 4. For all temperatures, the instantaneous strain hardening rate shows a linear dependence with respect to the reduced true stress $(\sigma-\sigma_y)$. It is clear that the work hardening rate regime is extended as the temperature decreases, and also the work hardening rate is higher for a given reduced true stress. To be precise, a high rate of strain hardening will postpone the necking, hence extending the formability of the sheet material. There is another effect for 6xxx observable: the formability decreases from RT to $-50\text{ }^{\circ}\text{C}$ and then increases again at $-100\text{ }^{\circ}\text{C}$ to RT level. From -100 to $-196\text{ }^{\circ}\text{C}$, the formability increases progressively. TEM investigations of microstructure are necessary to clarify this effect.

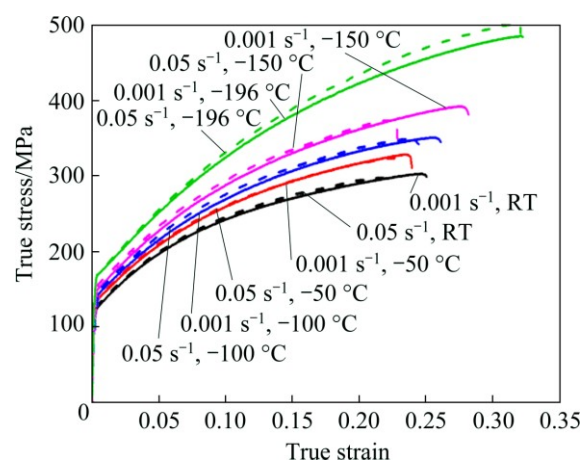


Fig. 3 Flow curves of AW-6016-T4 at different temperatures and strain rates

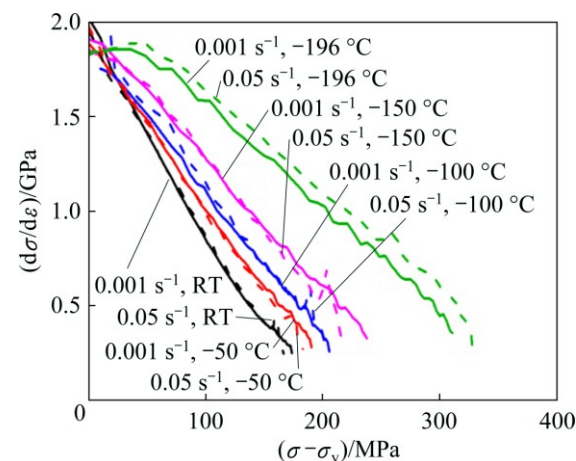


Fig. 4 Plot between instantaneous work hardening rate versus reduced true stress

Forming limit curves determined at RT, $-50\text{ }^{\circ}\text{C}$ and $-100\text{ }^{\circ}\text{C}$ are given in Fig. 5. There is a slight improvement in the major and minor strains from RT to $-100\text{ }^{\circ}\text{C}$, measured in the biaxial region. Insufficient lubrication at room temperature is probably the reason for the lower position of the point. The formability decreases from RT to $-50\text{ }^{\circ}\text{C}$ and then increases again at $-100\text{ }^{\circ}\text{C}$ to RT level for plain and uniaxial strain

condition (the same effect as in the tensile test). A suitable lubrication system could not be found for temperatures below $-100\text{ }^{\circ}\text{C}$, and this is a requirement for a pole failure in the Nakajima test (a crack-like defect is produced).

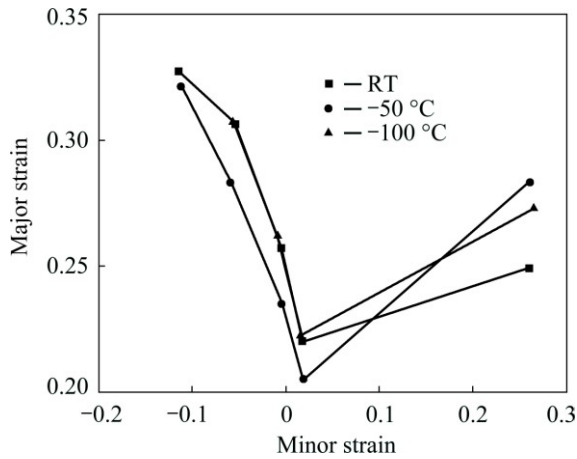


Fig. 5 Forming limit curves of AW-6016-T4 at different temperatures

Figure 6 indicates the stamping limit using various heights of the secondary design elements (see set-up in Fig. 1) at different testing temperatures. It can be seen that a stamping limit of 6 mm is reached at room temperature. If the AA6016 sheet is cooled down to $-150\text{ }^{\circ}\text{C}$, the secondary design element which indicates a height of 8 mm can be used for forming the B-pillar component without cracks. This formability enhancement correlates quite well with increasing uniaxial strain values if testing temperature is reduced to very low temperatures (Fig. 3).

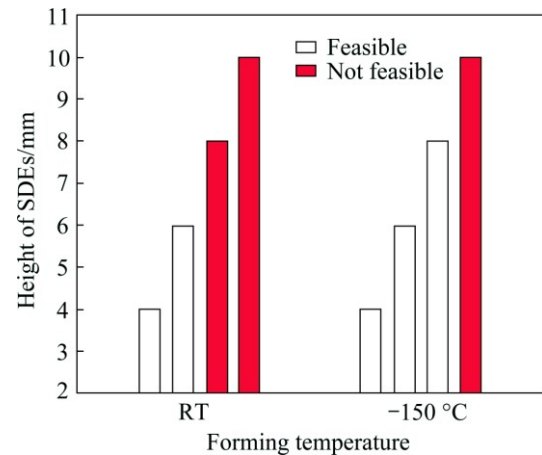


Fig. 6 Achievable heights of secondary design elements at different forming temperatures using AW-6016-T4 sheet material

From Fig. 7, the deformation structure is clearly visible in the deformed samples and not in the as-received one. The arrow below the figure shows the direction of tensile testing. The misorientation angles (2° – 5°) of EBSD scans (Fig. 8) can be used as an indication of localised plastic deformation, as shown by YU et al [12]. In Fig. 9, the fraction of misorientation angles calculated from Fig. 8 is shown, the deformation is clearly recognisable by the increase of the 2° – 5° portion to 0.55 at room temperature and 0.39 at $-196\text{ }^{\circ}\text{C}$. The total length of the small angle grain boundaries in the investigated area is approximately 12 mm after RT forming and about 9 mm after forming at $-196\text{ }^{\circ}\text{C}$.

It is known that the pronounced cross slip behaviour of aluminium at room temperature deformation causes

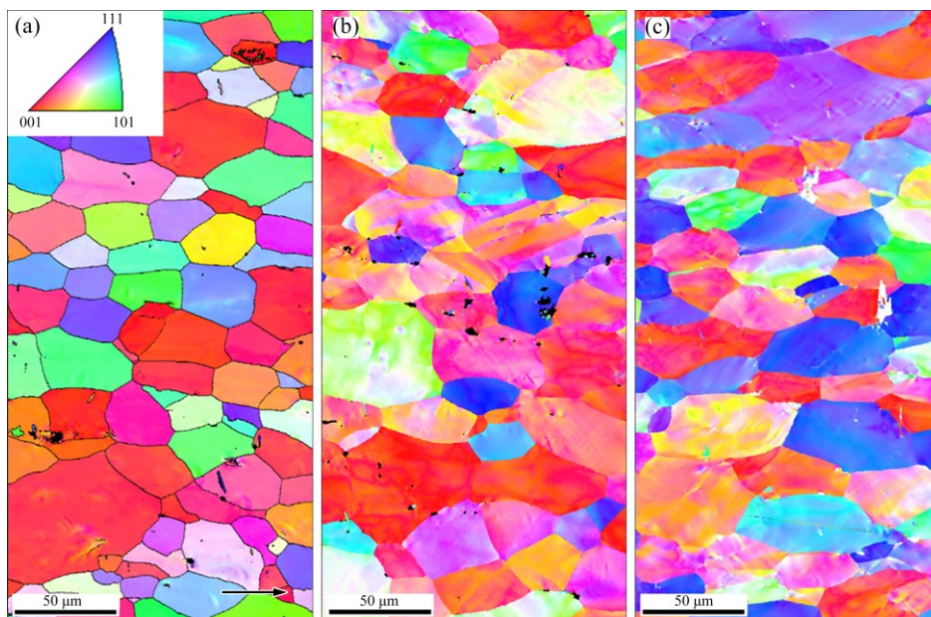


Fig. 7 IPF (inverse pole figure) maps of AW-6016-T4 samples parallel to tension direction (arrow): (a) As-received; (b) Deformed 20% at room temperature; (c) Deformed 20% at $-196\text{ }^{\circ}\text{C}$

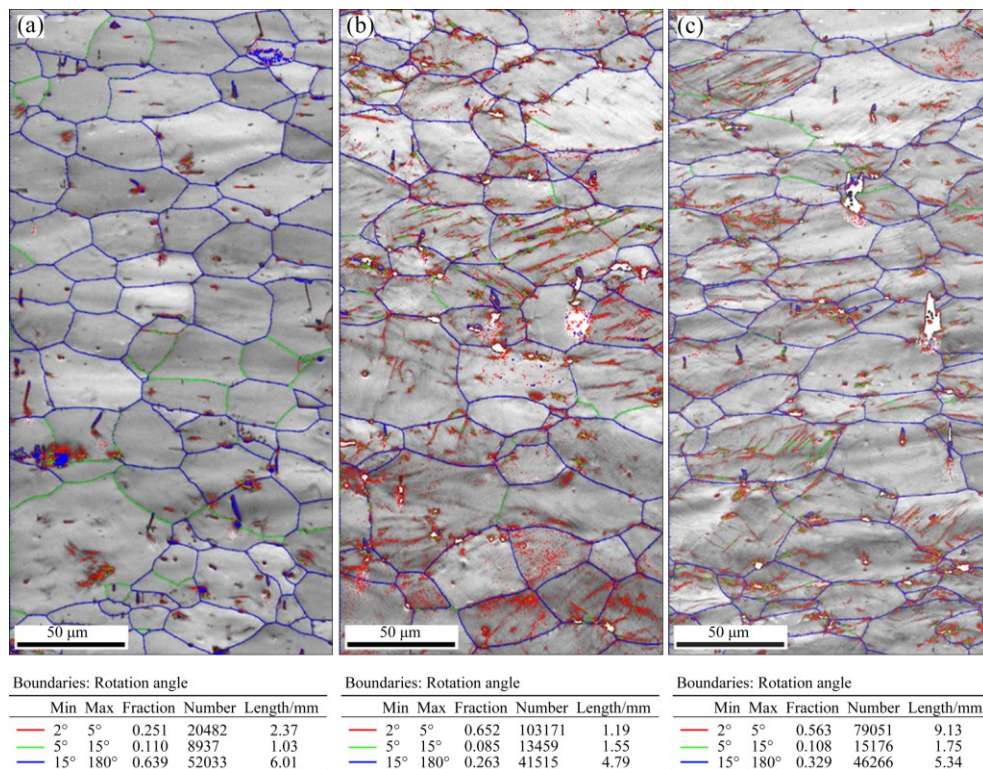


Fig. 8 Grain boundary misorientation maps of AW-6016-T4 samples parallel to tension direction: (a) As-received; (b) Deformed 20% at room temperature; (c) Deformed 20% at $-196\text{ }^{\circ}\text{C}$

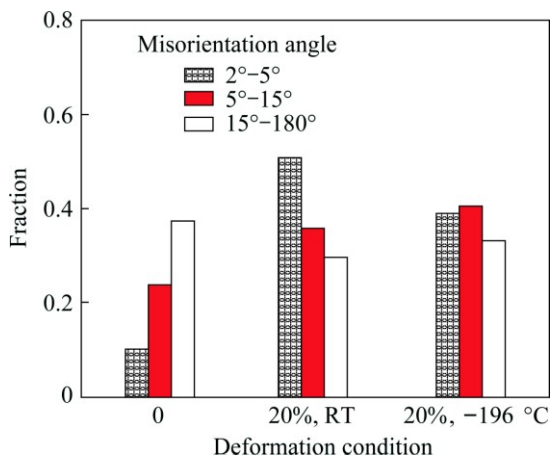


Fig. 9 Misorientation angles of EBSD scans in Fig. 8

dislocation cells formation [13]. The cells are separated by small-angle grain boundaries. Although the flow stress at the same degree of deformation is higher at cryogenic deformation temperatures than at room temperature, as shown in Fig. 3, less small-angle grain boundaries are formed due to suppressed cross slip at lower temperatures, hence, the deformation is more homogeneous.

DSC curves of the as-received sheet, the sheet deformed at room temperature and the sheet deformed at $-150\text{ }^{\circ}\text{C}$ are shown in Fig. 10. The endothermic and exothermic peaks in the resulting temperature vs heat

flow plots correspond to the dissolution and formation of precipitate, respectively. During the start of heating the as-received sheet in the T4 condition, an endothermic peak (peak 1) appears around $202\text{ }^{\circ}\text{C}$ relating to the dissolution of GP (Guinier–Preston) zone precipitates and indicates that these precipitates were present in the as-received AW-6016-T4 sheet. Further heating dissolves the GP zones and precipitation of the β'' phase occurs at $247\text{ }^{\circ}\text{C}$ (peak 2). These β'' phases further transform into β' phase (peak 3 at $290\text{ }^{\circ}\text{C}$). A small bulge is present at $335\text{ }^{\circ}\text{C}$ (peak 4). This bulge represents the precipitation of Si along with $\beta\text{-Mg}_2\text{Si}$ phase. Finally, all $\beta\text{-Mg}_2\text{Si}$ phase dissolves at $484\text{ }^{\circ}\text{C}$ (peak 5).

In the DSC curves of the deformed samples, the endothermic peak 1 (dissolution of GP zones) shifts to lower temperatures $187\text{ }^{\circ}\text{C}$. Exothermic peak 3 (precipitation of β') phase was also shifted to lower temperature bulge 3' around $270\text{ }^{\circ}\text{C}$. This shift shows that deformation of the samples accelerates the precipitation kinetics during heating in DSC run. The main reason for this is due to presence of higher amount of deformation-induced dislocations. Dislocations act as heterogeneous nucleation sites for precipitates and promote growth by short circuit diffusion. Therefore, we can observe a mixed nanostructure consisting of dislocations and precipitates in the deformed samples as described by KOLAR et al [14,15]. No shift of peak

temperature is observed for the dissolution of the β -Mg₂Si phase [14,16] and this suggests that these deformation-induced dislocations were annihilated before the dissolution of the β -Mg₂Si phase began.

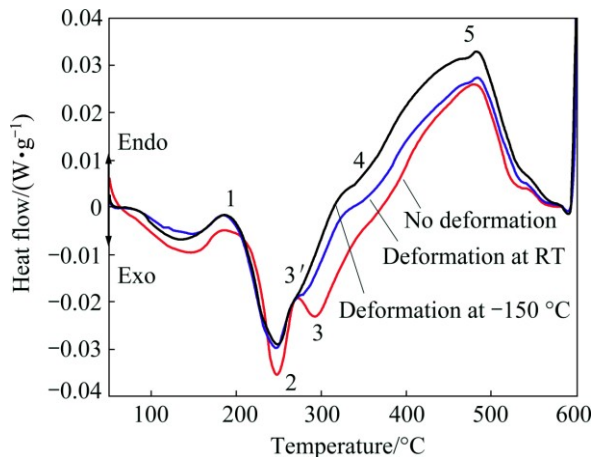


Fig. 10 DSC curves of AW-6016-T4 in un-deformed and deformed conditions

4 Conclusions

The improvement in the formability of aluminium alloys is generally obtained at elevated temperature. It causes the degradation in strength as well as quality of the formed parts. Cryogenic forming has shown improvement in both the strength and part quality. An automotive grade AW-6016-T4 sheet was characterized for cryo formability by tensile testing, Nakazima testing and finally forming a B-pillar part. The deformed microstructure was characterized by DSC and EBSD measurements. Significant improvement was found in elongation at fracture and strain hardening of AW-6016-T4 sheet at cryo temperature. EBSD measurements showed that the deformation at lower temperatures is more homogeneous. Further validation of improvement was shown by manufacturing a B-pillar part with variable side design elements of depth from 4–10 mm. A maximum depth of 6 mm was obtained during forming at RT while a maximum depth of 8 mm was reached during cryogenic forming at $-150\text{ }^{\circ}\text{C}$. This study has demonstrated the potential of cryogenic forming for manufacturing complex automotive components.

Acknowledgement

The authors would like to thank the Austrian Research Promotion Agency (FFG), the Federal Ministry for Transport, Innovation and Technology (bmvit) for sponsoring the project KryoAlu in the framework of Kooperative F&E-Projekte-Industrielle Forschung, Experimentelle Entwicklung. Special thanks to Dr. Nigel Ross and Dipl. Ing. Nikolaus Papenberg for helpful

discussion during the preparation of the manuscript.

References

- [1] DONNELL M O, BANABIC D, LEACOCK A G, BROWN D, MCMURRAY R J. The effect of pre-strain and inter-stage annealing on the formability of a 2024 aluminium alloy [J]. *International Journal of Material Forming*, 2008, 1: 253–256.
- [2] WANG K, HE B, CARSLY J E, RAGHAVAN R S, LI J, HARTFIELD-WÜNSCH S E. Structure–property characterization of an age hardenable Al–Mg–Si alloy after straining and flash annealing [J]. *Material Science and Engineering A*, 2014, 595: 25–33.
- [3] KUMAR M, ROSS N G. Influence of temper on the performance of a high-strength Al–Zn–Mg alloy sheet in the warm forming processing chain [J]. *Journal of Materials Processing Technology*, 2015, 231: 189–198.
- [4] GHOSH M, MIROUX A, WERKHOVEN R J, BOLT P J, KESTENS L A I. Warm deep-drawing and post drawing analysis of two Al–Mg–Si alloys [J]. *Journal of Materials Processing Technology*, 2014, 214: 756–766.
- [5] YING L U O, FRIEDMAN P, MING C, LIN G A O. Warm forming behavior of high strength aluminum alloy AA7075 [J]. *Transactions of Nonferrous Metals Society of China*, 2012, 22: 1–7.
- [6] FAN X, HE Z, ZHOU W, YUAN S. Formability and strengthening mechanism of solution treated Al–Mg–Si alloy sheet under hot stamping conditions [J]. *Journal of Materials Processing Technology*, 2016, 228: 179–185.
- [7] GARRETT R P, LIN J, DEAN T A. Solution heat treatment and cold die quenching in forming AA 6xxx sheet components: Feasibility study [J]. *Advanced Materials Research*, 2005, 8: 673–680.
- [8] KULAS M A, GREEN W P, TALEFF E M, KRAJEWSKI P E, MCNELLEY T R. Deformation mechanisms in superplastic AA5083 materials [J]. *Metallurgical and Materials Transaction A*, 2006, 37: 645–655.
- [9] SCHNEIDER R, GRANT R J, SOTIROV N, FALKINGER G, GRABNER F, REICHL C. Constitutive flow curve approximation of commercial aluminium alloys at low temperatures [J]. *Materials and Design*, 2015, 88: 659–666.
- [10] SOTIROV N, FALKINGER G, GRABNER F, SCHMID G, SCHNEIDER R, GRANT R J. Improved formability of AA5182 aluminium alloy sheet at cryogenic temperatures [J]. *Materials Today Proceedings*, 2015, 2: 113–118.
- [11] SCHNEIDER R, GRANT R J, HEINE B, BÖRRET R, BURGER S, ZOUAOUI Z. An analysis of the surface quality of AA5182 at different testing temperatures [J]. *Materials and Design*, 2014, 64: 750–754.
- [12] YU X, JIANG Z, ZHAO J, WEI D, ZHOU J. Local strain analysis of the tertiary oxide scale formed on a hot-rolled steel strip via EBSD [J]. *Surface Coating Technology*, 2015, 277: 151–159.
- [13] TAMLER H, KANERT O, ALSEM WHM, DE HOSSON J T M. Dislocation dynamics in aluminium and in aluminium-copper alloys: A nuclear magnetic resonance and transmission electron microscopic study [J]. *Acta Metallurgica*, 1982, 30: 1523–1536.
- [14] KOLAR M, PEDERSEN K O, GULBRANDSEN-DAHL S, TEICHMANN K, MARTHINSEN K. Effect of pre-deformation on mechanical response of an artificially aged Al–Mg–Si alloy [J]. *Materials Transaction*, 2011, 52: 1356–1362.
- [15] KOLAR M, PEDERSEN K O, GULBRANDSEN-DAHL S, MARTHINSEN K. Combined effect of deformation and artificial aging on mechanical properties of Al–Mg–Si Alloy [J]. *Transactions of Nonferrous Metal Society of China*, 2012, 22: 1824–1830.
- [16] NEMOUR H, MOURAD IBRAHIM D, TRIKI A. The effect of heavy cold plastic deformation on the non-isothermal kinetics and the precipitation sequence of metastable phases in an Al–Mg–Si alloy [J]. *Journal of Thermal Analysis and Calorimetry*, 2016, 123: 19–26.

AW-6016-T4 板材的低温成形行为

M. KUMAR¹, N. SOTIROV^{1,2}, F. GRABNER¹, R. SCHNEIDER³, G. MOZDZEN⁴

1. LKR Leichtmetallkompetenzzentrum Ranshofen GmbH,

Austrian Institute of Technology, Postfach 26, 5282 Ranshofen, Austria;

2. BENTELER Automobiltechnik GmbH, An der Talle 27-31, 33102 Paderborn, Germany;

3. Voestalpine Polynorm GmbH & Co. KG, Polynormstraße 1, 73529 Schwäbisch Gmünd, Germany;

4. Aerospace & Advanced Composites GmbH, Viktor-Kaplan-Strasse 2, 2700 Wiener Neustadt, Austria

摘 要: 研究析出强化 AW-6016-T4 金属板材的低温成形行为。利用拉伸和 Nakazima 测试方法获得材料在-196 至 25 °C 范围内的流变曲线和成形极限曲线。结果表明, 材料的强度和伸长率随温度的降低而增大。背散射电子衍射(EBSD)研究表明变形材料在室温和低温下显微组织有细微区别。但连续加热差热分析表明析出动力学之间无明显区别。本研究结果表明低温变形可用于制造 8 mm 深的 B 柱, 而常温变形只能制造 6 mm 深的 B 柱。

关键词: AW-6016-T4 合金; 低温成形; 应变硬化; 成形极限曲线

(Edited by Yun-bin HE)